Supporting Information

Electronic coupling engineering of FeF_2@FeNC heterostructure for highly efficient and robust alkaline oxygen reduction

Kang Liao[a], Shiyu Zhang[a], Sheng Zhao[a,b], Yixiao Zou[a], Jinfeng Zhang[a], Jiajun Wang[a], Xiaopeng Han[a,b,*]

a. School of Materials Science and Engineering, State Key Laboratory of Precious Metal Functional Materials, Tianjin University, Tianjin 300350, P. R. China

b. National Industry-Education Platform of Energy Storage, Tianjin University, Tianjin, 300350, P. R.China

Corresponding author: Xiaopeng Han

Email: xphan@tju.edu.cn

Table of Contents

Experimental section

Synthesis of Carbon Spheres.

Zinc acetate dihydrate (3.5 g), terephthalic acid (1.0 g), and polyvinyl alcohol (0.5 g) were dissolved in 50 mL of N,N dimethylformamide. The solution was transferred into a 100 mL Teflon lined autoclave and heated at 140 °C for 24 h in an electric oven. After cooling, the white precipitate was collected by centrifugation, washed three times with DMF, and dried at 80 °C for 48 h in a drying oven to obtain MOF-5 powder. Subsequently, 5 g of MOF-5 and 250 mg of melamine were mixed thoroughly. The mixture was placed in a corundum boat and transferred into a tube furnace. Under Ar atmosphere, the sample was heated to 950 °C at a ramp rate of 5 °C min^{-1}, held at this temperature for 3 h, and then furnace cooled to room temperature to obtain NC powder.

Synthesis of FeNC and Fe@FeNC.

Ferrous acetate (15 mg) and 1,10 phenanthroline (35 mg) were dissolved in 5 mL of methanol under stirring for 1 h until complete dissolution. Then, 50 mg of NC was added and the mixture was stirred for another 4 h. The solvent was removed using a rotary evaporator, and the obtained solid was transferred into a corundum boat and placed in a tube furnace. Under Ar atmosphere, the sample was heated to 800 °C at a ramp rate of 5 °C min^{-1}, held at this temperature for 2 h, and then furnace cooled to room temperature to obtain FeNC powder. The synthesis of Fe@FeNC was similar to that of FeNC, except that the amount of 1,10 phenanthroline was reduced to 6 mg.

Synthesis of FeF_2@FeNC.

Fe@FeNC powder (50 mg) and NH_4F (500 mg) were mixed thoroughly. The mixture was transferred into a corundum boat and placed in a tube furnace. Under Ar atmosphere, the sample was heated to 400 °C at a ramp rate of 5 °C min^{-1}, held at this temperature for 2 h, and then furnace cooled

to room temperature to obtain FeF_2@FeNC.

Materials characterization

The crystal structure and physical analysis of the synthesized materials were characterized by powder X-ray diffractometer (XRD, Bruker D8 Advanced, Cu Kα radiation, λ = 0.15418 nm). Raman spectra were collected using a Raman XploRA Plus from Horiba Scientific. Fourier Transform Infrared (FT-IR) spectroscopy were performed using Invenio S from Bruker. The morphology and nanostructure of the catalysts were observed using scanning electron microscopy (SEM, JEOL JEM-7610M, 15 kV) and energy dispersive spectrometry (EDS) as well as transmission electron microscopy (TEM, JEOL JEM-2100F, 200 kV). The single atom structure of catalysts was observed in detail by high-angle annular dark-field scanning transmission electron microscopy (HAADF-STEM, JEOL JEM-ARM200F, 200 kV) and double spherical aberration corrected transmission electron microscopy (DSAC-TEM, JEOL JEM-ARM300F2, 80 KV). XPS measurements were conducted using a Kratos AXIS Ultra X-ray photoelectron spectrometer. The Fe contents of the catalysts were determined by ICP-OES (Agilent 5110). Raman spectra were recorded on a Raman spectrometer (Raman XploRA Plus). The fine structure and coordination environment were detected by X-ray absorption spectroscopy (XAS, Shanghai Synchrotron Radiation Facility).

Electrochemical measurements

All the electrochemical measurements were carried out on an electrochemical workstation (Ivium-n-Stat, Ivium Technologies, Netherlands) in a standard three-electrode system at room temperature. All Potentials were converted to the reversible hydrogen electrode (RHE) scale using the equation:

$$E_{RHE} = E_{SCE} + 0.241V + 0.059pH$$

and the current densities were normalized to the geometric surface area.

To prepare the working electrode, 5 mg of the catalyst was dispersed into 970 μL ethanol and 30 μL Nafion under ultrasonication for 60 min to form the uniform ink. After that, 18 μL of the prepared ink was dropcast onto the working electrode in three aliquots, followed by natural drying. All the test were conducted in 0.1 M KOH (pH=13) lectrolyte that bubbled with O_2 or N_2 for 30 min before the measurement. Linear scanning voltammetry curves were measured for all samples at different rotation rates such as 400, 625, 900, 1225, 1600, 2025 round per minute (rpm). For the rotating disc electrode measurement, the kinetic current density (J_k) and electron transfer number (n) during the ORR process was determined by the Koutecky-Levich (K-L) equation:

$$\frac{1}{J} = \frac{1}{J_L} + \frac{1}{J_k} = \frac{1}{B\omega^{0.5}} + \frac{1}{J_k}$$

$$B = 0.62nFC_0(D_0)^{\frac{2}{3}}v^{-\frac{1}{6}}$$

Where J is the measured current density, J_L is the diffusion-limiting current density, ω is the angular velocity ($\omega=2\pi N$, N is rotating rate), n is electron transfer number, F is the Faraday constant (96485 C mol^{-1}), C_0 is the bulk concentration of O_2 (1.2×10^{-6} mol cm^{-3} for 0.1 M KOH), D_0 is the diffusion coefficient of O_2 (1.9×10-5 cm^2 s^{-1} in 0.1 M KOH), and v is the kinematic viscosity of the electrolyte (0.01 cm^2 s^{-1} in 0.1 M KOH). The hydrogen peroxide yield (H_2O_2 %) and the electron transfer number (n) were also calculated by the followed equations:

$$n = \frac{4 \times I_d}{\frac{I_d}{N} + I_r}$$

$$H_2O_2(\%) = \frac{200 \times I_r}{N \times I_d + I_r}$$

Where I_r and I_d are the measured ring and disk currents respectively. N is collecting efficiency (0.38)

of RRDE. The ring potential was set to 1.48 V vs. RHE.

Determination of Number of Fe Sites Involved in ORR Based on Redox Peak Method[1–3]

For FeF_2@FeNC catalyst (loading ~0.2 mg cm^{-2} on RDE, geometric area = 0.2475 cm^2):

Area oxidation peak

$= 0.049509\ \text{mA} \cdot \text{V}$

Convert to A·V:

$= 4.9509 \times 10^{-5}\ \text{A} \cdot \text{V}$

Charge associated with $Fe^{2+} \rightarrow Fe^{3+}$ oxidation (scan rate = 0.005 V s^{-1})

$$Q = \frac{4.9509 \times 10^{-5}\ \text{A} \cdot \text{V}}{0.005\ \text{V s}^{-1}} = 9.9018 \times 10^{-3}\ \text{A} \cdot \text{s} = 9.9018 \times 10^{-3}\ \text{C}$$

Charge of an electron = $1.602 \times 10^{-19}\ \text{C}$

Hence, number of electrons transferred

$$= \frac{9.9018 \times 10^{-3}\ \text{C}}{1.602 \times 10^{-19}\ \text{C}} = 6.18 \times 10^{16}$$

Since the Fe^{2+}/Fe^{3+} reaction is a single-electron transfer process, the number of electrons transferred equals the number of Fe–N_4 sites involved in the redox reaction. Therefore,

Number of Fe–N_4 sites that are electrochemically accessible

$= 6.18 \times 10^{16}$ Determination of Turnover Frequency (TOF) for ORR

Kinetic current at 0.85 V vs. RHE (from RDE, geometric area = 0.2475 cm^2, $j_k = 36.3\ \text{mA cm}^{-2}$):

$I_k = 36.3\ \text{mA cm}^{-2} \times 0.2475\ \text{cm}^2 = 8.98425\ \text{mA} = 8.98425 \times 10^{-3}\ \text{A}$

TOF at 0.85 V is given by:

$$\text{TOF} = \frac{I_k \times N_A}{4 \times F \times n_{\text{Fe}}}$$

Where $N_A = 6.022 \times 10^{23}\ \text{mol}^{-1}$, $F = 96485\ \text{C mol}^{-1}$, $n_{\text{Fe}} = 6.18 \times 10^{16}$, and the factor 4 accounts for the four-electron ORR pathway.

$$\text{TOF} = \frac{8.98425 \times 10^{-3} \times 6.022 \times 10^{23}}{4 \times 96485 \times 6.18 \times 10^{16}}$$

First, numerator: $8.98425 \times 10^{-3} \times 6.022 \times 10^{23} = 5.409 \times 10^{21}$

Denominator: $4 \times 96485 = 385940$; $385940 \times 6.18 \times 10^{16} = 2.385 \times 10^{22}$

Thus,

$$\text{TOF} = \frac{5.409 \times 10^{21}}{2.385 \times 10^{22}} = 0.227\ \text{s}^{-1}$$

The TOF values for FeNC and Fe@FeNC are calculated similarly, yielding 0.217 s^{-1} and 0.109 s^{-1}, respectively.

Fabrication of Zn–air battery

The Zn-air battery was fabricated using a home-made cell. The catalysts were loaded on the carbon cloth (1.0 ×1.0 cm^2) as air electrode. To prepare the air electrode, 5 mg of the catalyst or Pt/C with 5 mg IrO_2 were dispersed into a mixture of 950 μL of isopropyl alcohol and 50 μL of Nafion dispersion under ultrasonication for 2 h to form the uniform ink. After that, the prepared ink was dropped on the air electrode until the loading amount is around 2 mg cm^{-2}. A polished zinc foil was used as the anode. All the areas of the electrodes exposed to the electrolyte are 1 cm^2. The electrolyte was a mixture of 6.0 M KOH and 0.2 M $ZnAc_2$. The specific capacity and the gravimetric energy density were calculated on the mass of consumed Zn.

Calculation Method

All calculations in this work were conducted using the Vienna Ab-initio Simulation Package

(VASP), within the framework of spin-polarized Density Functional Theory (DFT). The Perdew-Burke-Ernzerh (PBE) of generalized-gradient approximation (GGA) functional is applied to model the electronic interactions[4–6]. Valence electron states were described using a plane-wave basis set with a cutoff energy of 500 eV, while core electrons were treated with Projector Augmented Wave (PAW) pseudopotentials. Van der Waals (vdW) interaction was considered at the DFT-D3 level as proposed by Grimme with Becke-Jonson damping method. The electronic convergence in the structural optimization is set with a force of 10^{-6} eV and 0.03 eV/Å. A vacuum layer with a height of 15 Å was established to prevent slab interactions and consider dipole correction to avoid surface polarization. To eliminate the spurious electrostatic interactions caused by periodic boundary conditions, a dipole correction was applied along the direction perpendicular to the surface (z axis). The k-mash for structural optimization was set to 3×3×1, and for calculating the DOS, it was enhanced to 6×6×1. Atomic charges were determined by Bader charge analysis. The COHP of considered atomic pairswas calculated by the Lobster code[7].

The dissolution energy (E_{diss}) of the Fe center, which assesses its stability against leaching, was calculated based on a thermodynamic cycle. It is defined as:

$$E_{diss} = E_{Defect-slab} + \mu_{Fe} - E_{slab}$$

Where E_{slab} is the total energy of the pristine catalyst slab model, $E_{Defect\text{-}slab}$ is the total energy of the slab after removal and structural re-optimization of the Fe atom, and μ_{Fe} is the chemical potential of a dissolved Fe atom, approximated here by the energy per atom in bulk bcc iron. A positive E_{diss} value indicates an endothermic dissolution process, reflecting stability against leaching.

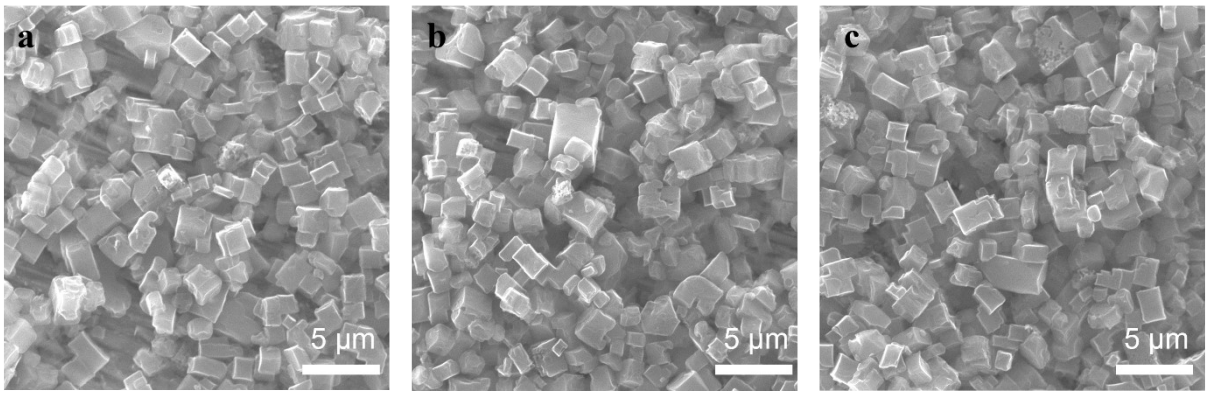

Fig. S1. The SEM images of (a) FeNC, (b) Fe@FeNC and (c) FeF_2@FeNC catalysts.

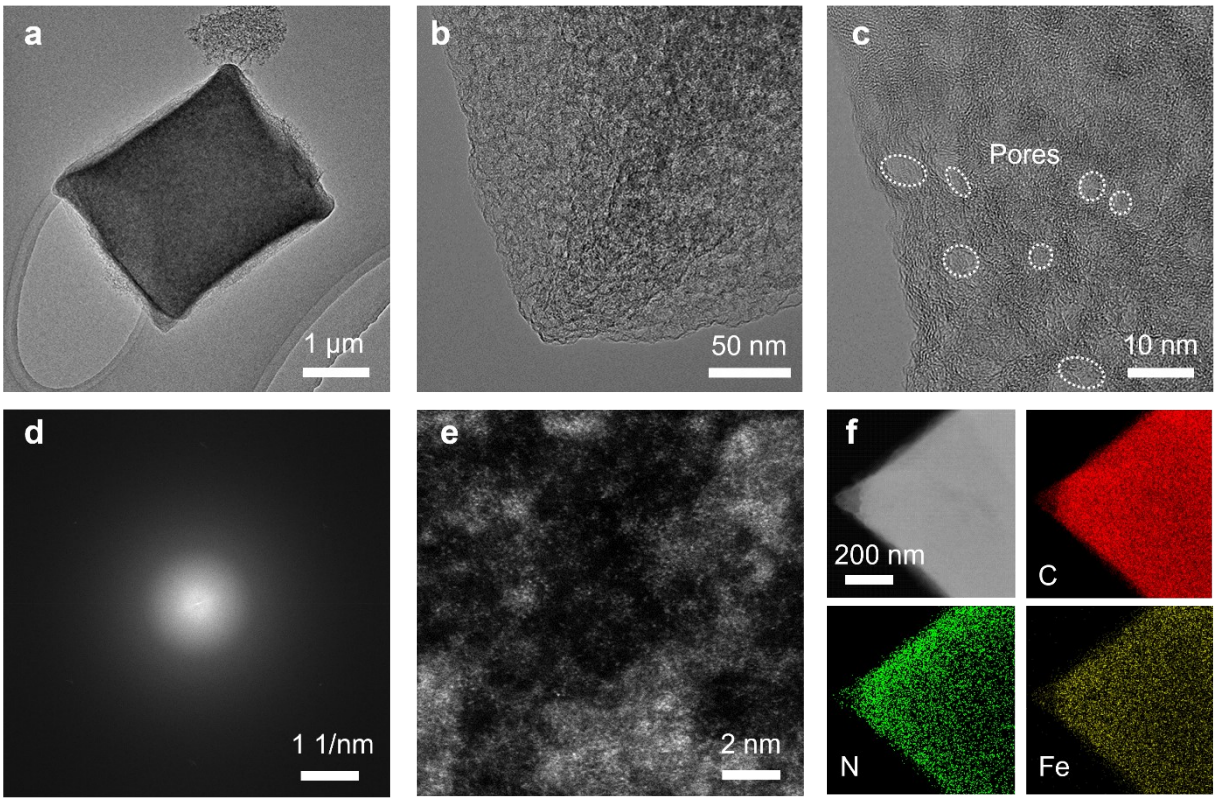

Fig. S2. (a) and (b) TEM images, (c) HRTEM image, (d) SEAD image, (e) AC HAADF STEM image, (f) HAADF STEM images and corresponding EDS elemental maps of FeNC.

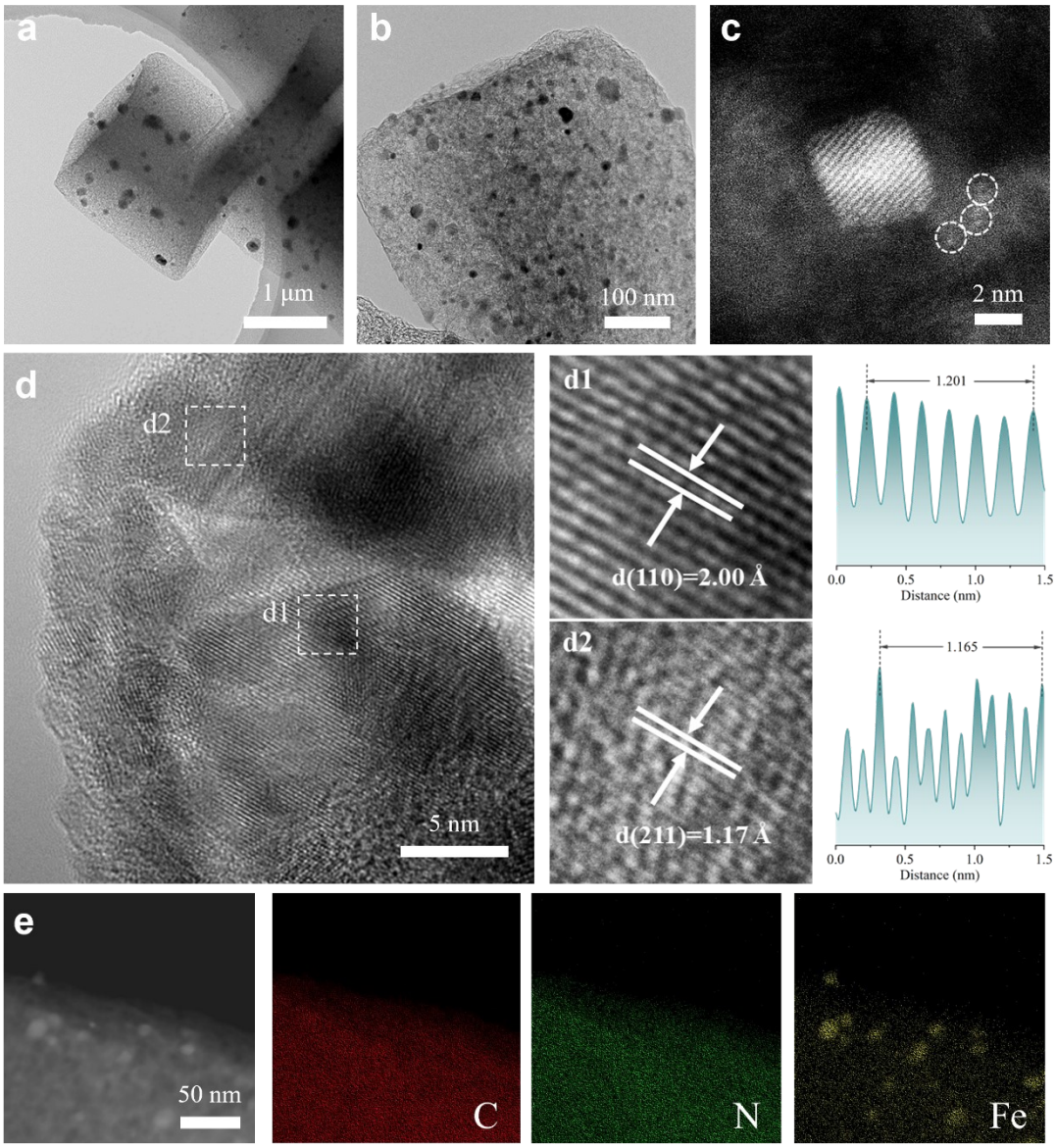

Fig. S3. The (a) and (b) TEM images, (c) AC HAADF STEM image, (d) HRTEM image, (e) HAADF STEM images and corresponding EDS elemental maps of Fe@FeNC.

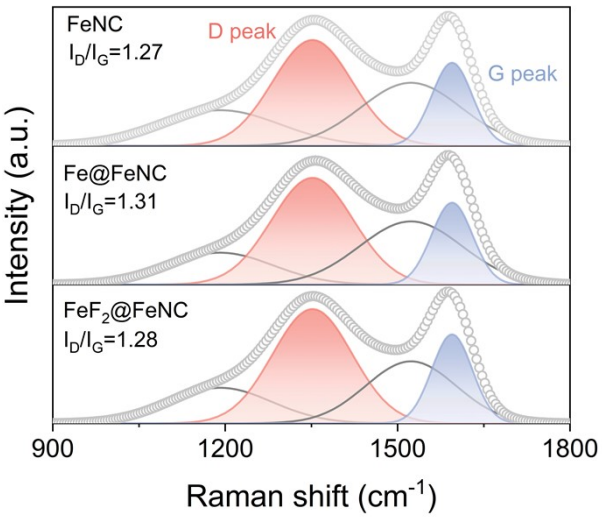

Fig. S4. The Raman spectra of FeNC, Fe@FeNC and FeF_2@FeNC.

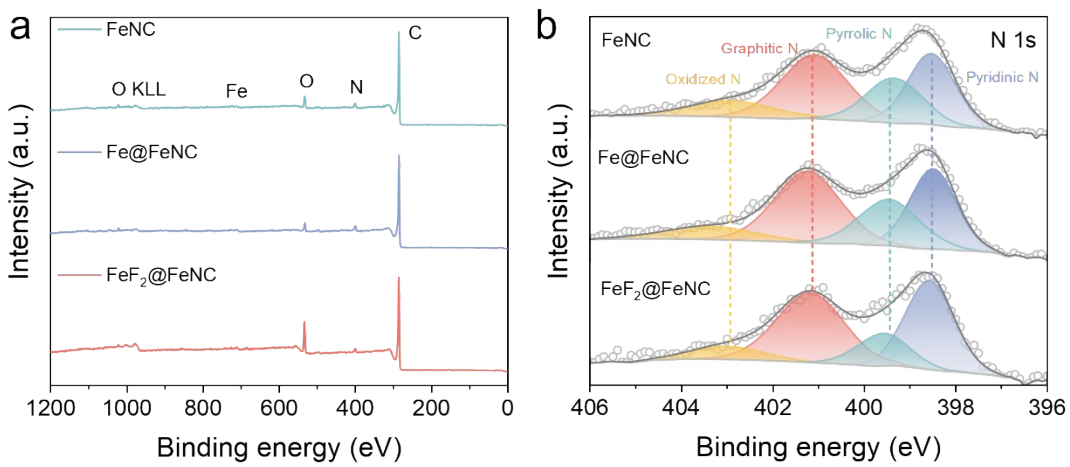

Fig. S5. (a) The survey XPS spectra and (b) N 1s spectra of FeNC, Fe@FeNC and FeF_2@FeNC.

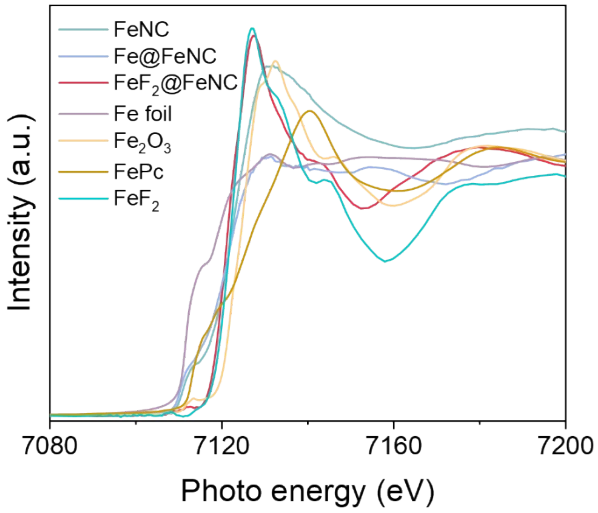

Fig. S6 The normalized Fe K-edge XANES curves of FeNC, Fe@FeNC, FeF_2@FeNC, Fe foil, Fe_2O_3, FePc, FeF_2 samples.

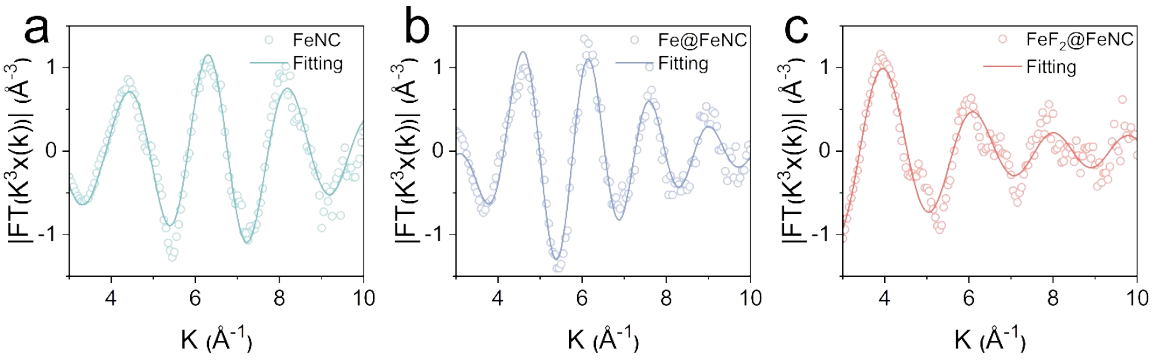

Fig. S7. Fitting curves in k space of (a) FeNC, (b) Fe@FeNC and (c) FeF_2@FeNC.

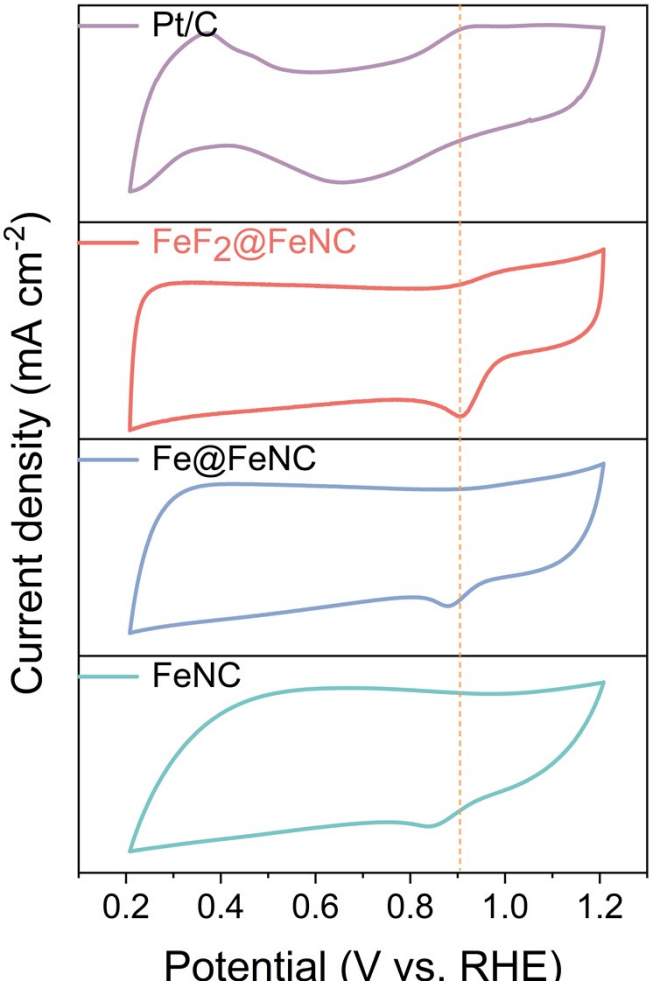

Fig. S8. The CV curves of FeNC, Fe@FeNC, FeF_2@FeNC and Pt/C catalysts.

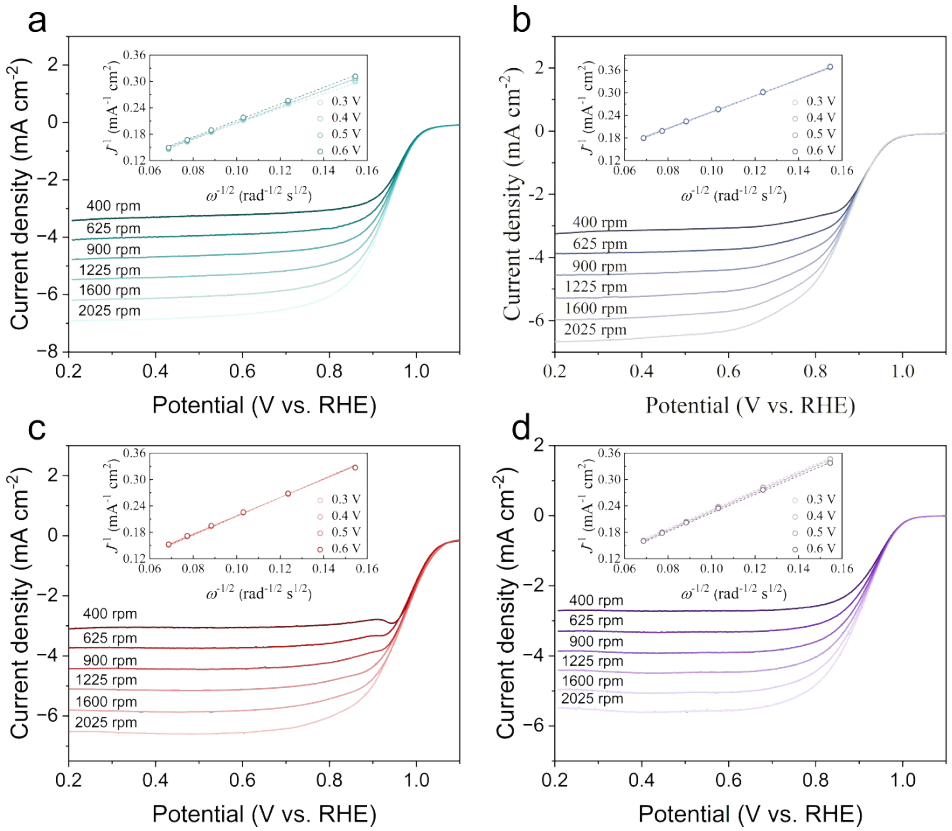

Fig. S9. The LSV curves of (a) FeNC, (b) Fe@FeNC, (c) FeF_2@FeNC and (d) Pt/C at different rotating speeds. Inserts show corresponding K-L plots at different potential.

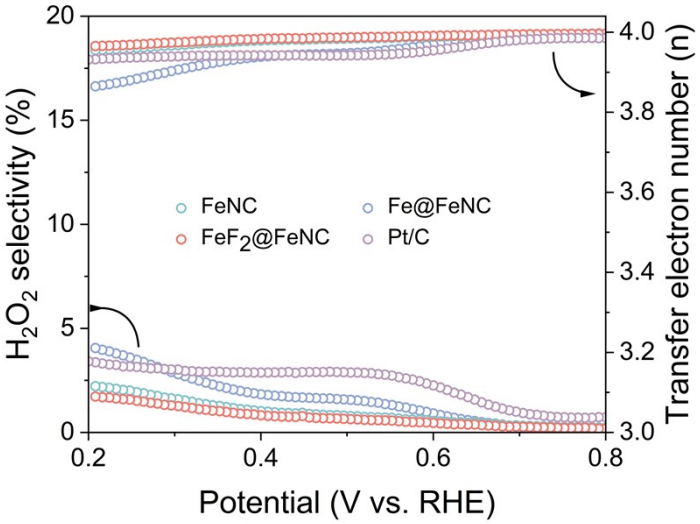

Fig. S10. The H_2O_2 selectivity and electron transfer number of FeNC, Fe@FeNC, FeF_2@FeNC and Pt/C.

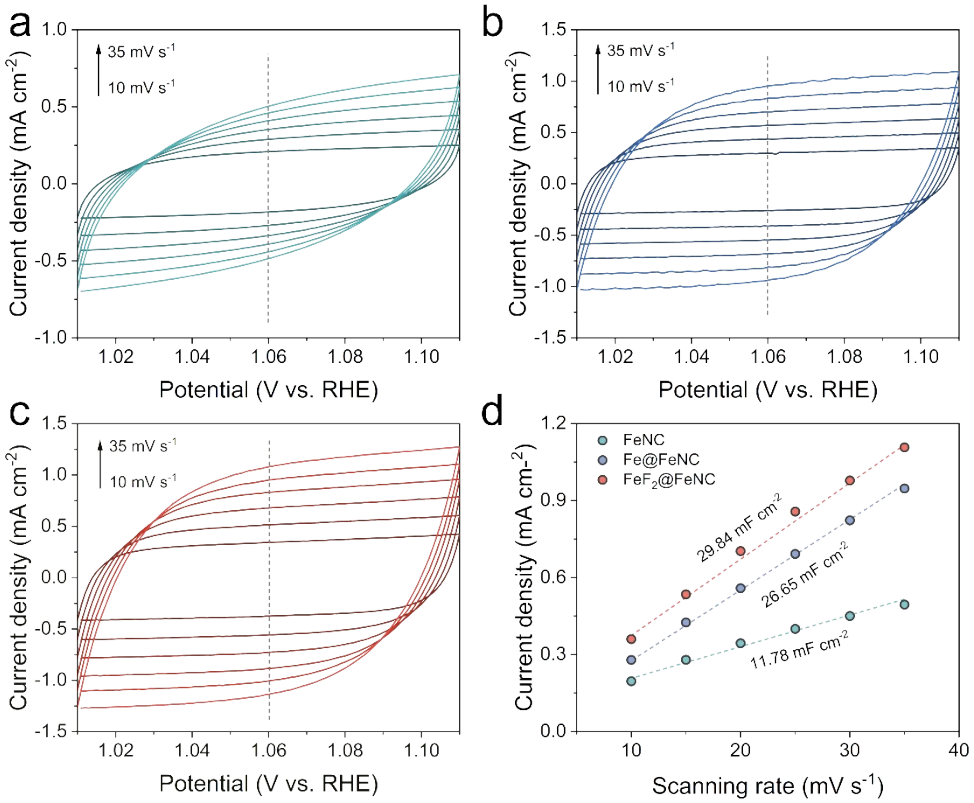

Fig. S11. The CV curves of (a) FeNC, (b) Fe@FeNC and (c) FeF_2@FeNC at different sweep speeds. (d) Fitting results for C_{dl} at 1.06 V.

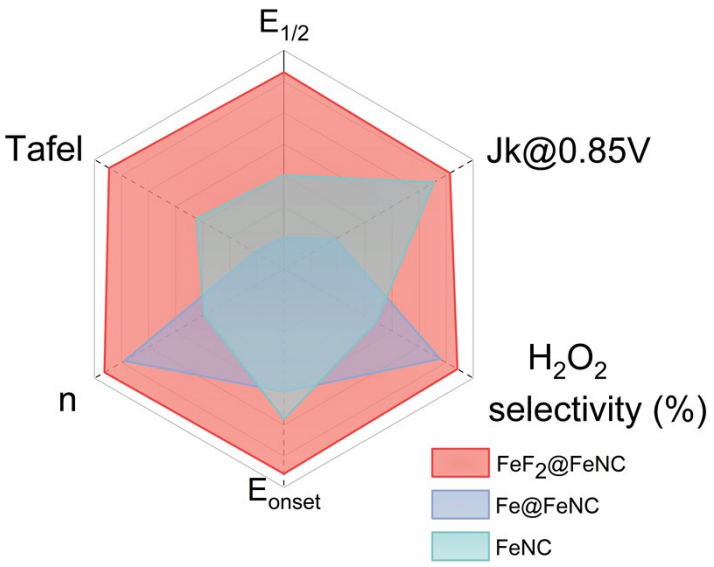

Fig. S12. Radar plot comparing the ORR performance for FeNC, Fe@FeNC and FeF_2@FeNC.

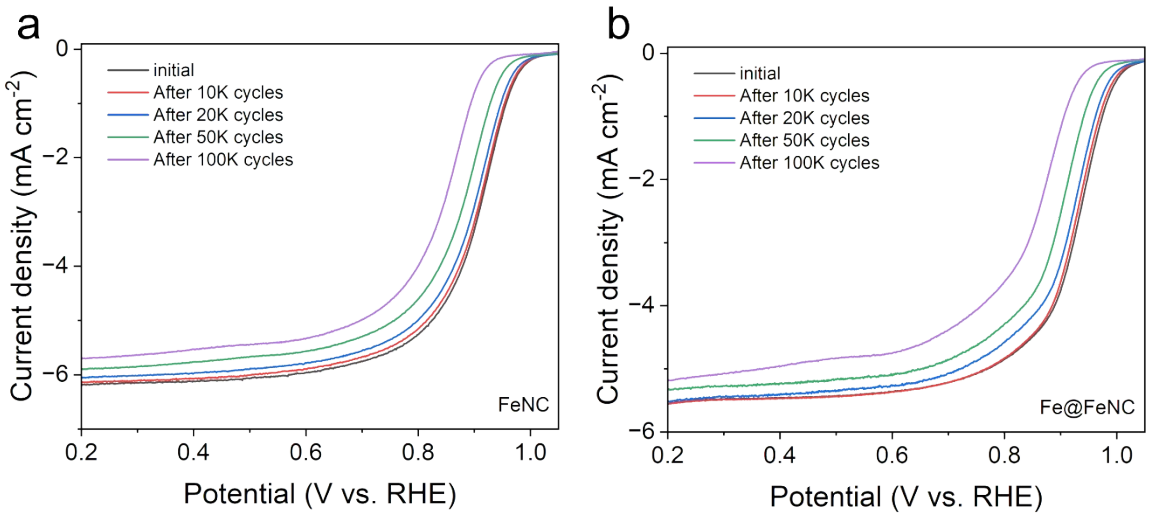

Fig. S13. The LSV curves before and after 10K, 20K, 50K and 100Kcycles of (a) FeNC and (b) Fe@FeNC.

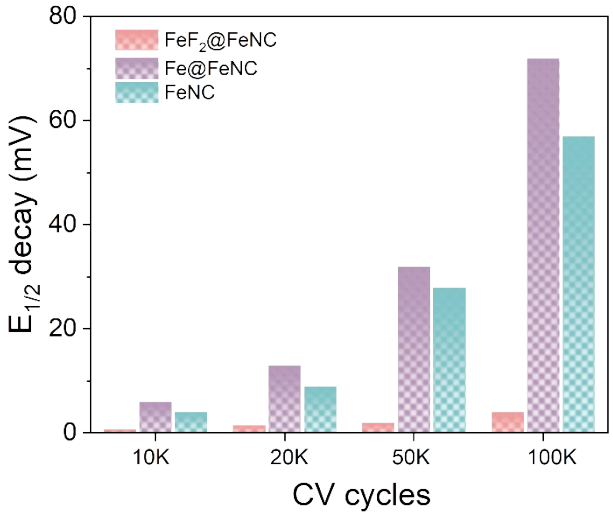

Fig. S14. The half-wave potential decay values for FeF_2@FeNC, Fe@FeNC, and FeNC catalysts after 10k, 20k, 50k, and 100k ADT cycles.

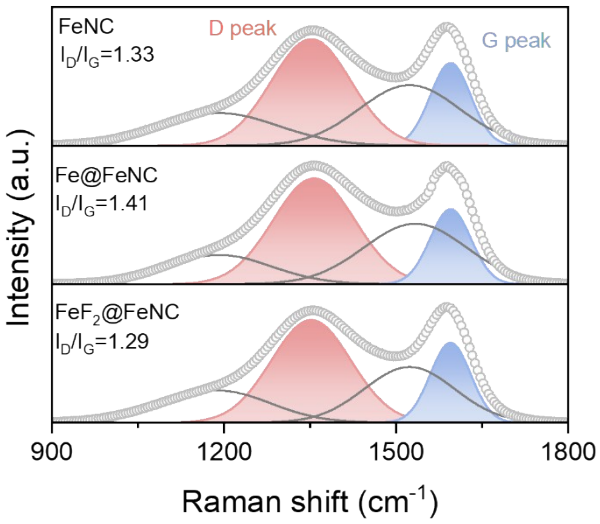

Fig. S15 The Raman spectra of FeNC, Fe@FeNC and FeF_2@FeNC recorded after 50,000 accelerated durability test (ADT) cycles.

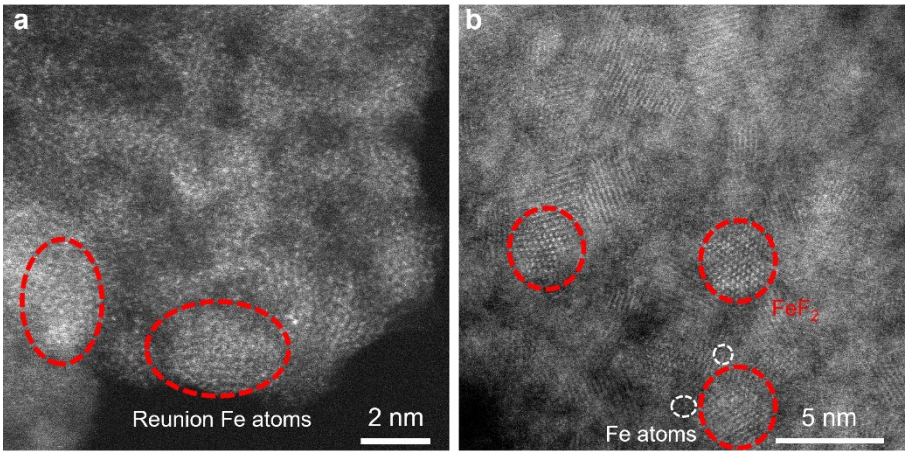

Fig. S16 AC HAADF HRTEM image of (a) FeNC and (b)FeF_2@FeNC after 50000 ADT cycles test.

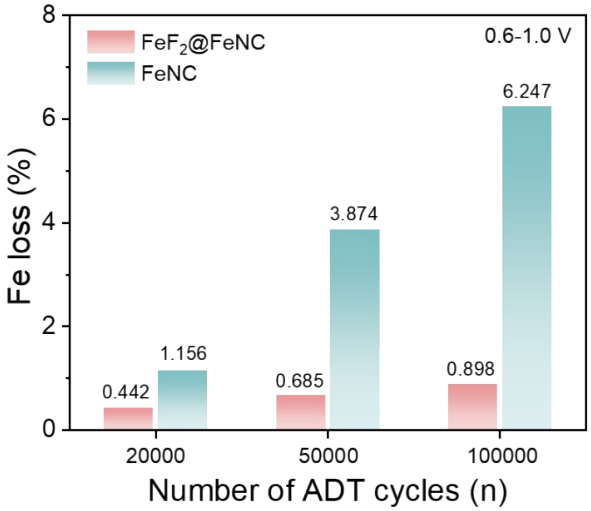

Fig. S17 The Fe content loss of FeNC and FeF_2@FeNC after ADT cycling between 0.6 and 1.0 V.

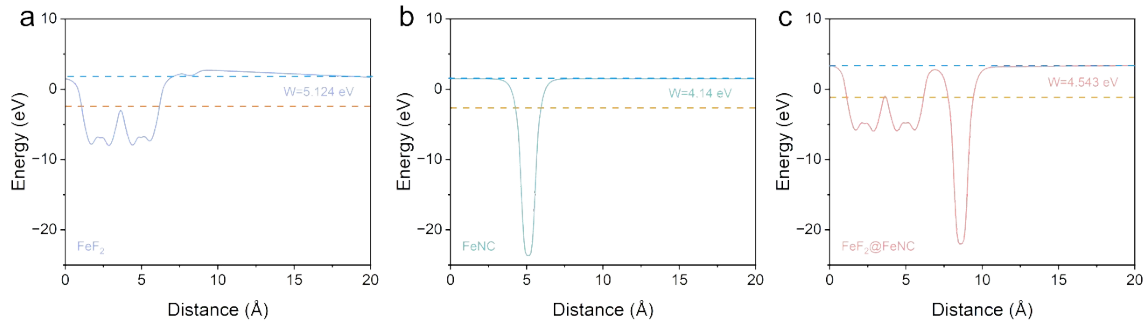

Fig. S18. The Calculated work functions of (a) FeF_2, (b) FeNC and (c) FeF_2@FeNC.

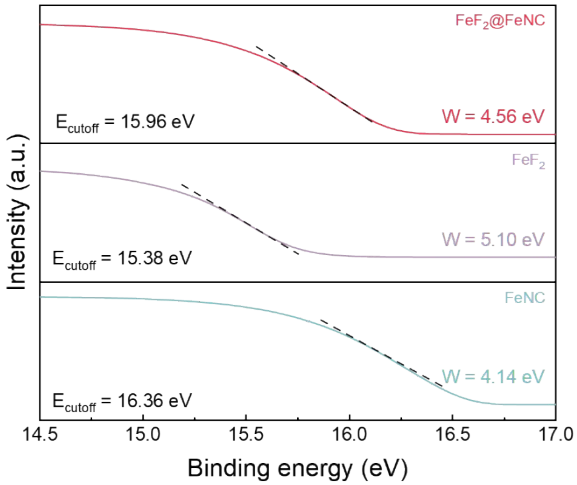

Fig. S19 The UPS curves of FeNC, FeF_2 and FeF_2@FeNC samples.

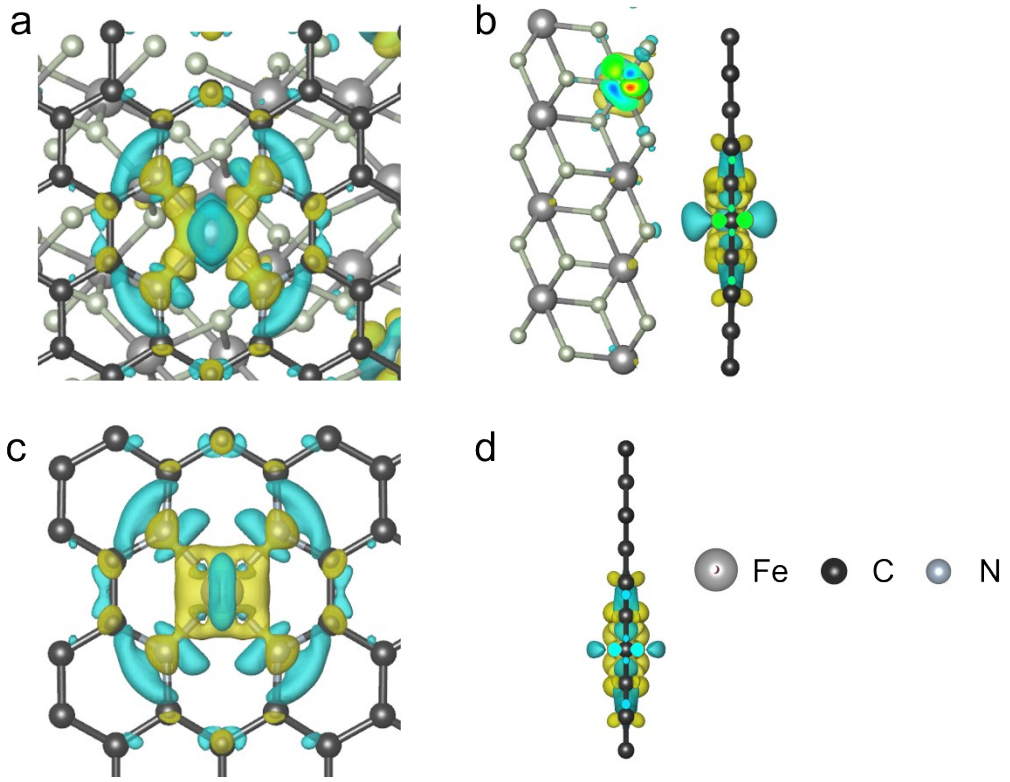

Fig. S20. The three-dimensional differential charge density of (a,b) FeF_2@FeNC and (c,d) FeNC.

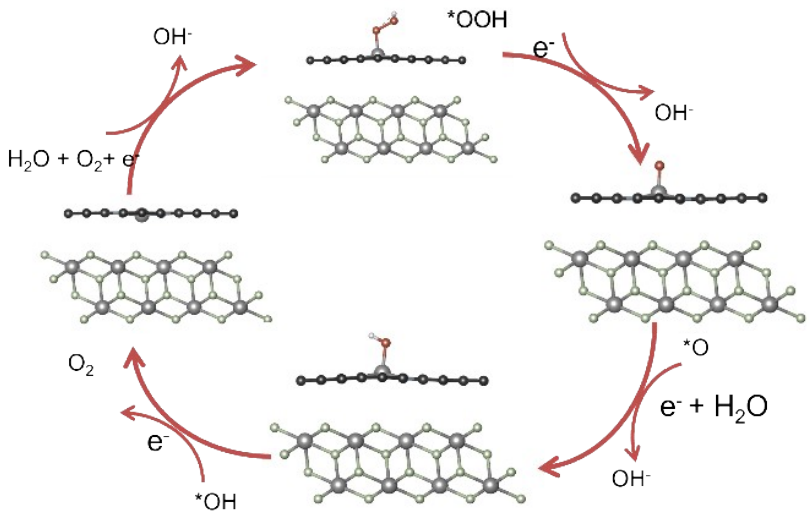

Fig. S21. The Proposed ORR elemental steps for FeF_2@FeNC.

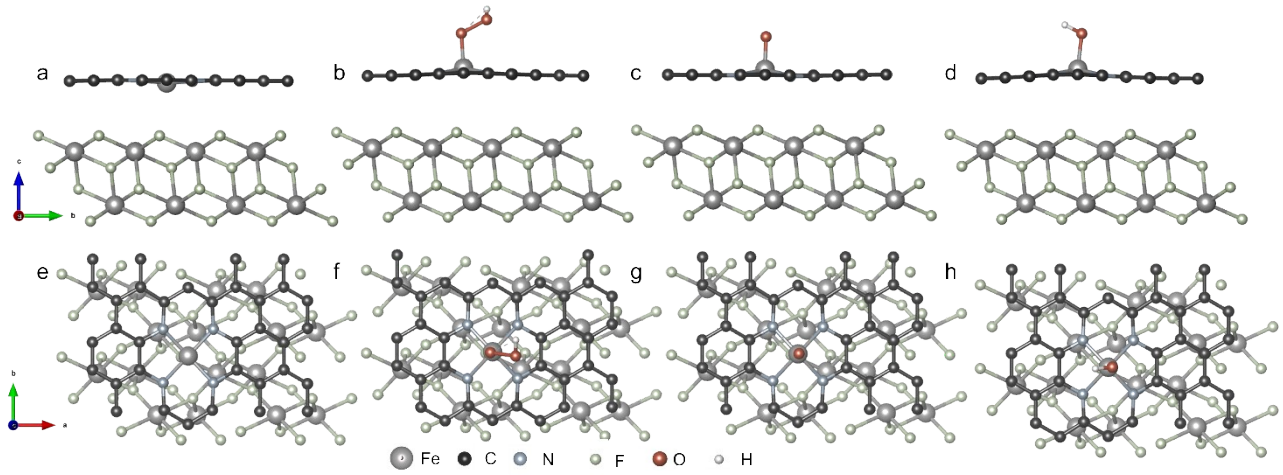

Fig. S22. Optimized structures of ORR intermediates on FeF_2@FeNC. (a–d) Side views of the slab model, *OOH, *O, and *OH, respectively. (e–f) Top views of the slab model and *OH, respectively.

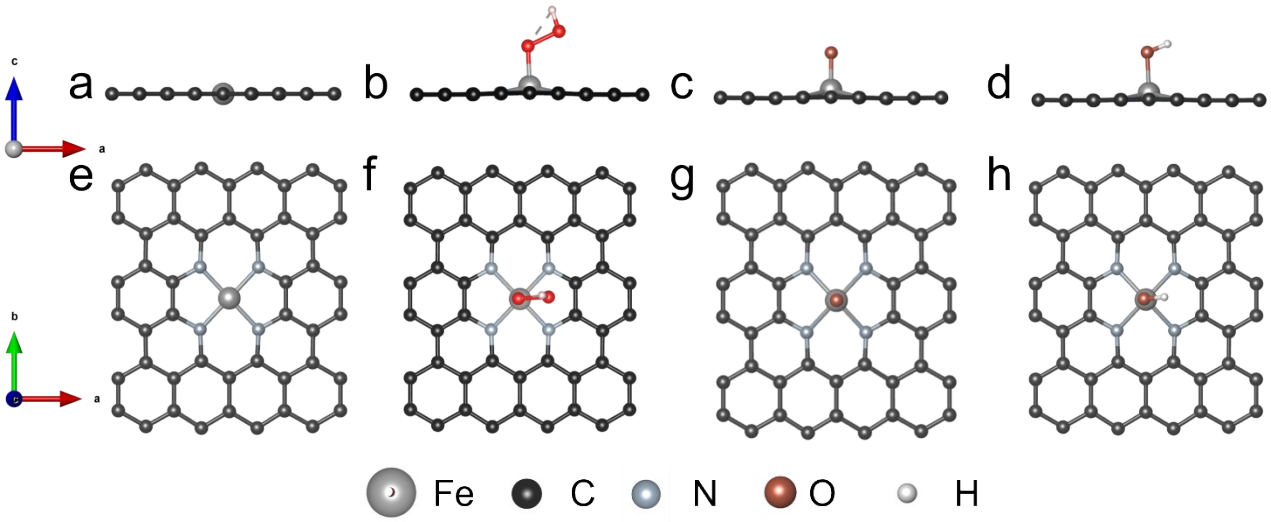

Fig. S23. Optimized structures of ORR intermediates on FeNC. (a–d) Side views of the slab model, *OOH, *O, and *OH, respectively. (e–f) Top views of the slab model and *OH.

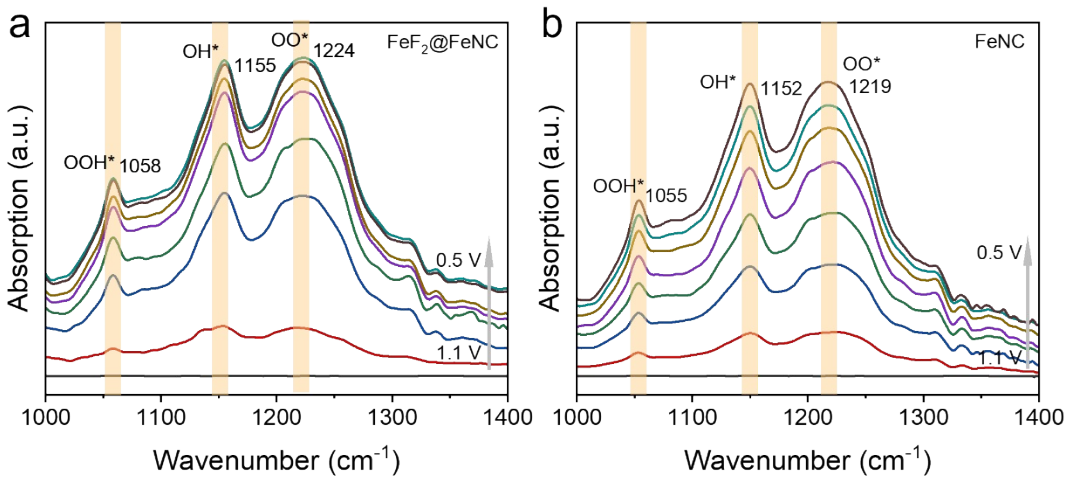

Fig. S24 The in-situ FT-IR spectra for FeF_2@FeNC and FeNC.

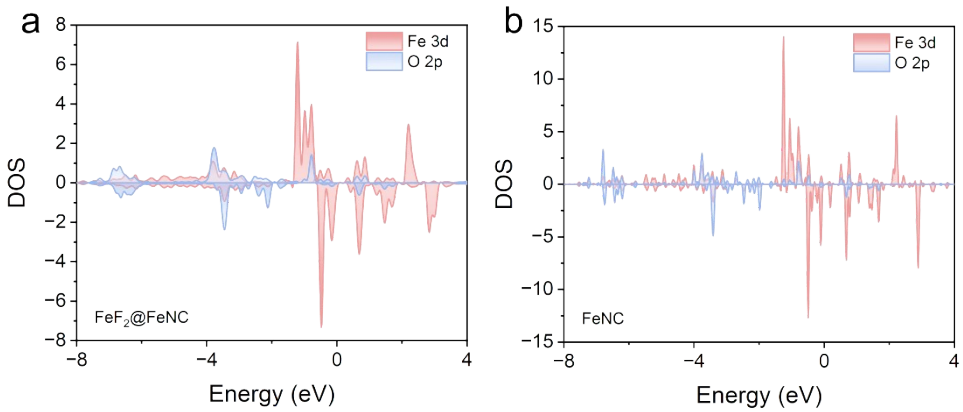

Fig. S25. The Projected density of states (PDOS) of Fe 3d and O 2p orbitals after *OH adsorption on (a) FeF_2@FeNC and (b) FeNC.

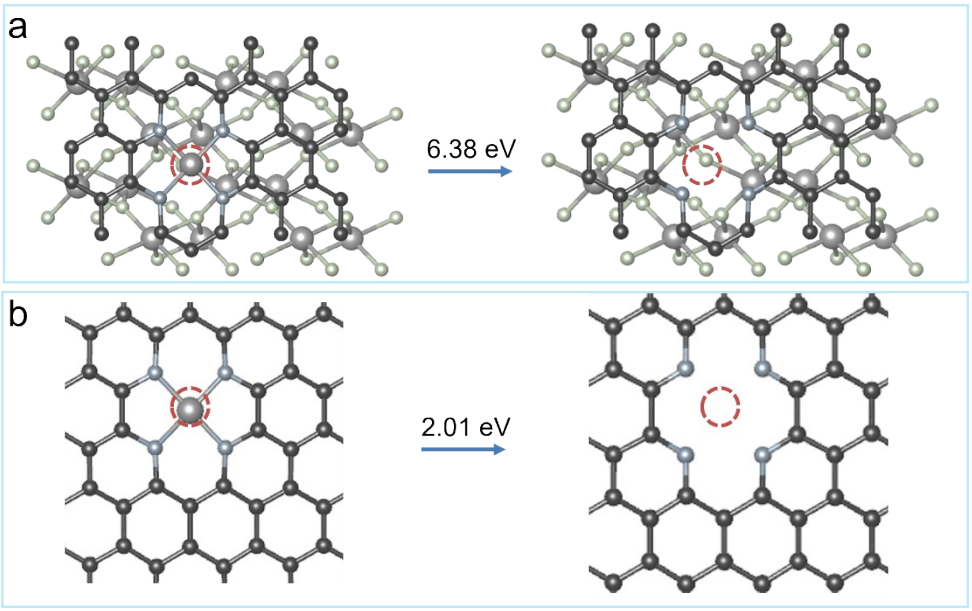

Fig. S26. The dissolution energy of (a) FeNC and (b) FeF_2@FeNC.

Table S1. The Fe contents of FeF_2@FeNC, Fe@FeNC and FeNC determined by ICP-OES.

Sample	FeF_2@FeNC	Fe@FeNC	FeNC
Fe (wt. %)	2.86	3.11	2.53

Table S2. EXAFS fitting parameters at the Fe K-edge for FeF_2@FeNC, Fe@FeNC and FeNC.

Sample	Path	CN	R(Å)	σ^2(Å^2)	ΔE_0	R factor
FeF_2@FeNC	Fe-N	3.98	1.92	0.009	8.169	0.012
	Fe-F	5.92	2.03	0.003		
Fe@FeNC	Fe-N	3.95	1.97	0.015	-6.565	0.007
	Fe-Fe	7.97	2.56	0.012		
FeNC	Fe-N	3.99	1.98	0.007	5.243	0.011

CN is the coordination number; R is the interatomic distance (the bond length between central atoms and surrounding coordination atoms); ΔE_0 is an edge–energy shift (the difference between the zero kinetic energy value of the sample and that of the theoretical model); σ^2 is Debye–Waller factor (a measure of thermal and static disorder in absorber–scatter distances); R factor is used to value the quality of the fitting.

Table S3.ORR performances of FeNC, Fe@FeNC, FeF_2@FeNC and Pt/C.

Sample	E_{onset} (V vs. RHE)	$E_{1/2}$ (V vs. RHE)	J_k (mA cm-2)
FeNC	0.99	0.91	18.2
Fe@FeNC	1.01	0.93	33.8
FeF_2@FeNC	1.05	0.96	36.3
Pt/C	1.00	0.87	9.7

The E_{onset} is defined as the potential at which the reduction current reaches 5% of the limiting diffusion current.

Table S4. Comparison of ORR performance of carbon–supported catalysts.

Catalysts	E_{onset} (V vs. RHE)	$E_{1/2}$ (V vs. RHE)	Reference
FeF_2@FeNC	1.05	0.96	This work
FeF_2@FeNC after 300K ADT	1.05	0.95	This work
Co_2/Fe–N@CHC	1.03	0.915	[8]
FeN_4-Fe_{NCP}@MCF	1.02	0.894	[9]
Ni,FeDSAs/NCs	1.04	0.895	[10]
$Fe_{SA/AC}$@HNC	0.99	0.90	[11]
FePNC	1.01	0.90	[12]
Fe_2N_5P	0.96	0.86	[13]
FeSNC-TA	1.01	0.91	[14]
Fe,Ni/NC@NG	0.949	0.858	[15]
SA-Fe^{III}/SNPC	0.99	0.91	[16]
Fe-SA/N-HCS	1.02	0.91	[17]
Fe_{SA}/N,S-PHLC	0.97	0.91	[18]
FeN4-Te_n	0.922	0.867	[19]
FeNC-2M	0.986	0.897	[20]
CoFeCu-TAC	0.975	0.84	[21]
Fe–N,O/G	1.00	0.86	[22]
Fe-ACSA@NC	1.03	0.90	[23]
FeN/Fe_3C@CNS,	1.02	0.91	[24]
Fe,N,P-CNSs/Fe_2P	0.955	0.854	[25]
Fe_1-$NS_{1.3}C$	0.97	0.86	[26]

References

1 Y. Hao, D. Yu, S. Zhu, C.-H. Kuo, Y.-M. Chang, L. Wang, H.-Y. Chen, M. Shao and S. Peng, *Energy Environ. Sci.*, 2023, **16**, 1100–1110.

2 S. Anantharaj and S. Kundu, *ACS Energy Lett.*, 2019, **4**, 1260–1264.

3 S. Anantharaj, P. E. Karthik and S. Noda, *Angew Chem Int Ed*, 2021, **60**, 23051–23067.

4 B. Hammer, L. B. Hansen and J. K. Nørskov, *Phys. Rev. B*, 1999, **59**, 7413–7421.

5 G. Kresse and J. Furthmüller, *Computational Materials Science*, 1996, **6**, 15–50.

6 G. Kresse and D. Joubert, *Phys. Rev. B*, 1999, **59**, 1758–1775.

7 R. Dronskowski and P. E. Bloechl, *J. Phys. Chem.*, 1993, **97**, 8617–8624.

8 Z. Wang, X. Jin, C. Zhu, Y. Liu, H. Tan, R. Ku, Y. Zhang, L. Zhou, Z. Liu, S. Hwang and H. J. Fan, *Advanced Materials*, 2021, **33**, 2104718.

9 Z. Wang, Z. Lu, Q. Ye, Z. Yang, R. Xu, K. Kong, Y. Zhang, T. Yan, Y. Liu, Z. Pan, Y. Huang and X. Lu, *Adv Funct Materials*, 2024, **34**, 2315150.

10 Z. Wang, X. Jin, R. Xu, Z. Yang, S. Ma, T. Yan, C. Zhu, J. Fang, Y. Liu, S.-J. Hwang, Z. Pan and H. J. Fan, *ACS Nano*, 2023, **17**, 8622–8633.

11 H. Zhang, H. Chen, S. Feizpoor, L. Li, X. Zhang, X. Xu, Z. Zhuang, Z. Li, W. Hu, R. Snyders, D. Wang and C. Wang, *Advanced Materials*, 2024, **36**, 2400523.

12 H. Liu, L. Jiang, Y. Sun, J. Khan, B. Feng, J. Xiao, H. Zhang, H. Xie, L. Li, S. Wang and L. Han, *Advanced Energy Materials*, 2023, **13**, 2301223.

13 Q. Miao, Z. Chen, X. Li, M. Liu, G. Liu, X. Yang, Z. Guo, C. Yu, Q. Xu and G. Zeng, *ACS Catal.*, 2023, **13**, 11127–11135.

14 H. Liu, L. Jiang, Y. Sun, J. Khan, B. Feng, J. Xiao, H. Zhang, H. Xie, L. Li, S. Wang and L. Han, *Adv Funct Materials*, 2023, **33**, 2304074.

15 Q. Jing, Z. Mei, X. Sheng, X. Zou, Q. Xu, L. Wang and H. Guo, *Adv Funct Materials*, 2024, **34**, 2307002.

16 J. Wang, C. Hu, L. Wang, Y. Yuan, K. Zhu, Q. Zhang, L. Yang, J. Lu and Z. Bai, *Adv Funct Materials*, 2023, **33**, 2304277.

17 L. Zong, K. Fan, L. Cui, F. Lu, P. Liu, B. Li, S. Feng and L. Wang, *Angew Chem Int Ed*, 2023, **62**, e202309784.

18 M. Yuan, Y. Liu, Y. Du, Z. Xiao, H. Li, K. Liu and L. Wang, *Adv Funct Materials*, 2024, **34**, 2401484.

19 B. Ji, J. Gou, Y. Zheng, X. Zhou, P. Kidkhunthod, Y. Wang, Q. Tang and Y. Tang, *Advanced Materials*, 2022, **34**, 2202714.

20 C. Shao, J. Hua, Q. Li, Y. Xia, L. Sun, L. Wang and B. Li, *Nano Energy*, 2024, **126**, 109668.

21 J. Zhong, Z. Liang, N. Liu, Y. Xiang, B. Yan, F. Zhu, X. Xie, X. Gui, L. Gan, H. B. Yang, D. Yu, Z. Zeng and G. Yang, *ACS Nano*, 2024, acsnano.3c08839.

22 Y. Li, Y. Ding, B. Zhang, Y. Huang, H. Qi, P. Das, L. Zhang, X. Wang, Z.-S. Wu and X. Bao, *Energy Environ. Sci.*, 2023, **16**, 2629–2636.

23 H. Huang, D. Yu, F. Hu, S. Huang, J. Song, H. Chen, L. L. Li and S. Peng, *Angew Chem Int Ed*, 2022, **61**, e202116068.

24 Y. Wang, T. Yang, X. Fan, Z. Bao, A. Tayal, H. Tan, M. Shi, Z. Liang, W. Zhang, H. Lin, R. Cao, Z. Huang and H. Zheng, *Angew Chem Int Ed*, 2024, **63**, e202313034.

25 R. Ma, X. Cui, X. Xu, Y. Wang, G. Xiang, L. Gao, Z. Lin and Y. Yang, *Nano Energy*, 2023, **108**,

108179.
26 Z. Chen, H. Niu, J. Ding, H. Liu, P. Chen, Y. Lu, Y. Lu, W. Zuo, L. Han, Y. Guo, S. Hung and Y. Zhai, *Angewandte Chemie*, 2021, **133**, 25608–25614.